LABORATORY INVESTIGATION

USCAP UNITED STATES AND CANADIAN ACADEMY OF PATHOLOGY
Creating a Better Pathologist

Research Article

Unstained Tissue Imaging and Virtual Hematoxylin and Eosin Staining of Histologic Whole Slide Images

Sonja Koivukoski[a], Umair Khan[b], Pekka Ruusuvuori[b,c], Leena Latonen[a,d,*]

[a] Institute of Biomedicine, University of Eastern Finland, Kuopio, Finland; [b] Institute of Biomedicine, University of Turku, Turku, Finland; [c] Faculty of Medicine and Health Technology, Tampere University, Tampere, Finland; [d] Foundation for the Finnish Cancer Institute, Helsinki, Finland

ARTICLE INFO

ABSTRACT

Tissue structures, phenotypes, and pathology are routinely investigated based on histology. This includes chemically staining the transparent tissue sections to make them visible to the human eye. Although chemical staining is fast and routine, it permanently alters the tissue and often consumes hazardous reagents. On the other hand, on using adjacent tissue sections for combined measurements, the cell-wise resolution is lost owing to sections representing different parts of the tissue. Hence, techniques providing visual information of the basic tissue structure enabling additional measurements from the exact same tissue section are required. Here we tested unstained tissue imaging for the development of computational hematoxylin and eosin (HE) staining. We used unsupervised deep learning (CycleGAN) and whole slide images of prostate tissue sections to compare the performance of imaging tissue in paraffin, as deparaffinized in air, and as deparaffinized in mounting medium with section thicknesses varying between 3 and 20 μm. We showed that although thicker sections increase the information content of tissue structures in the images, thinner sections generally perform better in providing information that can be reproduced in virtual staining. According to our results, tissue imaged in paraffin and as deparaffinized provides a good overall representation of the tissue for virtually HE-stained images. Further, using a pix2pix model, we showed that the reproduction of overall tissue histology can be clearly improved with image-to-image translation using supervised learning and pixel-wise ground truth. We also showed that virtual HE staining can be used for various tissues and used with both 20× and 40× imaging magnifications. Although the performance and methods of virtual staining need further development, our study provides evidence of the feasibility of whole slide unstained microscopy as a fast, cheap, and feasible approach to producing virtual staining of tissue histology while sparing the exact same tissue section ready for subsequent utilization with follow-up methods at single-cell resolution.

Introduction

Histology is the cornerstone method to assess tissue structures, phenotypes, and pathology. The histologic workflow includes tissue fixation, embedding, sectioning, and mounting on coverslips. The initially transparent sections are typically stained

---

* Corresponding author.
E-mail address: leena.latonen@uef.fi (L. Latonen).

chemically to visualize them with colors for overall tissue phenotype examination, most commonly with hematoxylin and eosin (HE). Hematoxylin, once oxidized, is a positively charged dye that stains basophilic structures, such as nuclei and ribosomes, blue, whereas eosin is a negatively charged dye staining most other cellular organelles pink. Through differences in staining intensity, HE staining is thus capable of displaying a wide range of morphologic structures with great detail, making it the standard stain combination used in routine pathology.[1]

The chemical staining procedures are often irreversible, preventing the use of the same tissue section for other purposes afterward. Hence, for most traditional approaches, the tissue is sectioned into multiple sections used for different stainings or other assays individually. This, however, does not allow assessment of several properties in same cells as, depending on the section thickness, each section contains material from mostly different cells.

Recent methodologic development of spatial molecular methods, such as spatial transcriptomics, allows single-cell and even subcellular resolution of macromolecules and are thus useful in assessing cellular heterogeneity in tissues and disease.[2] With current protocols, the reference staining, such as HE, needs to be performed from a neighboring section.[3] This hampers the accuracy in relating the overall tissue structure and pathologic identification of cells to the molecular, subcellular information. To overcome this caveat in the current technologies, the same tissue section should be used for both overall tissue investigation and spatial, molecular assays. To achieve this, visualization of the tissue should be performed without an irreversible chemical staining. If the chemical staining could be computationally created, tissue sections could be imaged in an unstained, transparent mode prior to molecular assessments and visualized in silico. Development of such virtual staining approaches requires associating the information content in images of HE-stained sections with that of the unstained sections and developing computational methods to virtually create the stained representative of an image of an unstained tissue section.

Virtual HE staining of unstained tissue images can be categorized as an image-to-image translation problem, which is a well-known problem area in computer vision. Deep learning-based image-to-image translation has proven to be efficient in generating synthetic images translated from one domain to another.[4] Such an approach for virtual histologic staining requires both unstained and stained tissue images as training data. The association between these can be facilitated either in a supervised manner through pixel-wise correspondence or in an unsupervised manner through learning the style without a direct pixel-wise match between the source and the target domains. Information from adjacent or nearby histologic tissue sections is not fully aligned owing to the 3-dimensional structure of tissue; hence, an unsupervised approach is used here for such data. Unsupervised image-to-image translation methods[5-8] use techniques such as cycle consistency loss[5] for learning image mapping. CycleGAN is the most commonly used unsupervised method for image-to-image translation. It employs an adversarial training technique, in which 2 components, a generator and a discriminator, train in a 0-sum manner to generate and detect synthetic images, respectively.[9] CycleGAN, however, consists of 2 pairs of generators and discriminators, 1 pair for each-way translation, ie, A-to-B and B-to-A.[6] The method was first used to translate natural images, whereas in medical imaging, the method and its variants have been successfully applied in magnetic resonance to computer tomography image synthesis.[10-13] In computational pathology, CycleGAN has been established as a tool for cross-stain translation[14-16] and domain adaptation or stain transformation.[17,18] The supervised image-to-image translation methods[19-22] require paired or registered data[23] for training. Thus far, only a few studies experimented with traditional light microscopy on unstained tissues for virtual HE staining.[24,25]

In this study, we used CycleGAN for transforming unstained tissue section images acquired from multiple experimental setups into virtually stained HE images. We experimentally optimized and streamlined the sample processing and imaging pipeline to enable efficient virtual HE staining. We tested different tissue section thicknesses and 3 different ways to prepare the sections for imaging to identify the best-suited protocol for virtual staining. Further, with the optimized tissue section thickness and imaging protocol, we used the pix2pix method, which is a conditional adversarial network variant used for supervised image-to-image translation,[19] to show increased histologic accuracy and applicability of virtual staining to various tissues with supervised deep learning. We imaged unstained tissue sections with standard brightfield imaging technology available in practically any lab. Our results validated a viable method for unstained tissue imaging and virtual HE staining of histologic whole slide images (WSIs) and presented a way to record and visualize the overall tissue structures from a tissue section in ways that spare the tissue intact for usage in follow-up measurements.

Materials and Methods

Tissue Samples

Tissues of wild-type FVB/N mice were used. The PAXgene-fixed (PreAnalytiX GmbH), paraffin-embedded anterior lobe of mouse prostate was cut into 3-, 5-, 8-, 12-, and 20-μm-thick sections. Formalin-fixed, paraffin-embedded liver, kidney, and testis were cut into 5-μm-thick sections. The tissue sections were placed on glass slides and attached by incubation in +37 °C for 30 minutes. The paraffin was removed with xylene, after which the tissue was rehydrated with absolute and 96% ethanol and dipped in distilled water. HE staining was continued immediately after rehydration with Delafield Hematoxylin (reference number: 1159380100; Merck), followed by running tap water, adding 120-mM HCl in 70% ethanol, running tap water, and adding eosin (reference number: 1159350025; Merck). The staining was followed by dehydration with 96% absolute ethanol and xylene. Coverslips were attached with a mounting medium (DPX Mountant for Histology, reference number: 06522; Sigma). Adjacent sections of each thickness were processed in the following 4 different ways: 1 without any processing after attaching to slides, 1 with paraffin removal and rehydration, 1 with paraffin removal, rehydration, dehydration, and mounting of the coverslip, and 1 with standard HE staining, which includes all the steps of the above protocol. The tissue material used originates from prior studies,[26-28] in which all animal experimentation and care procedures were performed in accordance with guidelines and regulations of the national Animal Experiment Board of Finland and were approved by the board of laboratory animal work of the State Provincial Offices of South Finland (license number: ESAVI/6271/04.10.03/2011).

Imaging

Imaging was performed using Thunder Imager 3D Tissue slide scanner (Leica Microsystems) equipped with DMC2900 camera (Leica Microsystems) and HC PL APO 40x/0.95 DRY and HC PL

FLUOTAR 20x/0.5 DRY objectives (Leica Microsystems) with differential interference contrast using Kohler illumination. The light source was white light-emitting diode, with the refractive index being set as 1, and the mounting medium refractive index as 1.457. WSIs were stitched together with LAS X (ver 3.7.4.; Leica Microsystems). The pixel size of the acquired WSIs was 0.353 μm for 40×, and 0.671 μm for 20×, and the images were stored as tiff files.

Unsupervised Virtual Staining Algorithm

For training, all unstained tissue images and their HE-stained reference tissue images were split horizontally such that both halves had the same amount of tissue content. The bottom halves were used for training the CycleGAN model, and the top halves were used for testing its performance on the virtual staining task. For training, the WSIs were split into 256 x 256 pixel tiles with a stride size of 128 pixels in both x and y directions to ensure a significant overlap.

Random tile sampling was employed for each training WSI. Altogether, 16,000 tiles were used for the training. All models were trained for 40 epochs, with a batch size of 4. For every epoch, 25% of the image tiles were randomly augmented on the fly, including flipping, rotation, and scaling.

For inference, epochs with the lowest generator loss were chosen. Because Generative Adversarial Networks (GANs) are challenging to train, and the lowest loss does not always translate to the best image quality, multiple epochs were chosen. For inference, a tile size of 2048 × 2048 pixels and a stride of 512 pixels in both x and y directions were used. Because the generator model was fully convolutional, it allowed changing the tile size as per the requirements. Experiments have shown that increased tile size during inference results in more uniform instance normalization tile statics, which help to alleviate the tiling effect.[17]

Statistical Evaluation

Frachet inception distance (FID) score was used for statistical evaluation.[29] FID score is used to measure the distance between 2 distributions of images, typically when one set is real and the other is virtually generated. In practice, the FID score is calculated on feature vectors extracted from both sets of images. In the case of virtual staining, InceptionV3[30] was used to extract the bottleneck features, a vector of 2048 dimensions. Feature-wise mean and covariance matrix were computed on both reference HE tiles and virtually stained HE tiles. The FID score was computed using the following equation:

$$d^2 = |\mu_X - \mu_Y|^2 + tr\left(\sum X + \sum Y - 2\left(\sum X \sum Y\right)^{1/2} \right),$$

where d^2 represents the FID score, μ_X and μ_Y are the means, and $\sum_X$ and $\sum_Y$ are the covariance matrices of the real and virtually stained image tiles, respectively.

Supervised Virtual Staining Algorithm

A conditional adversarial network[19] is a supervised learning method for generating synthetic data using learning mapping from input to output image. This study used a variant of a conditional adversarial network called pix2pix for supervised image-to-image translation. The pix2pix model consists of a U-net−based generator[31] and a PatchGAN-based discriminator.[19] Because pix2pix is a supervised method, it requires the data from the 2 domains to be first aligned with a pixel-level correspondence between the images of each individual image pair. Along with the GAN loss, pix2pix also employs an additional L1 loss term for the generator network by maximizing the use of the aligned data, thus producing better-quality translated images as compared with unsupervised learning methods.

In addition to the preprocessing steps used in unsupervised virtual staining experiments, the unstained and HE-stained images were aligned through an image registration process, which is essential for supervised virtual staining experiments. The number of tiles used for training varied depending on the size of the tissue; for instance, for the testis, 50,000 tiles were used, whereas for the liver, 35,000 tiles were used for training. Models were trained for 50 epochs. The tile size was also increased from 256 × 256 to 512 × 512 for model training.

With liver tissue, different image magnifications were experimented with during inference. A model was trained on tissue images captured with a 20× objective and used to virtually stain an unstained tissue image captured with the same objective to compare it with the 40× experiment results. In a separate experiment, a model trained with tissue images captured at 40× was fed an unstained tissue image captured with a 20× objective during inference. This was followed by upsampling the 20× objective image to 40× during inference.

Model Training Duration

The training time varied depending on the type of model, quantity of data, number of graphics processing units (GPUs), and number of training epochs. For instance, the pix2pix model for the anterior prostate was trained with 125,000 tiles (4 samples), for 50 epochs, over 4 GPUs, and the training was completed in approximately 16 hours. For the CycleGAN model, which is significantly larger than pix2pix model, the training was completed in approximately 31 hours for the anterior prostate with 3-μm section thickness and coverslipped samples, with 40,000 tiles, for 40 epochs, and over 1 GPU. All the models were trained on Tesla V100 GPUs (NVidia).

Histologic Evaluation

For visual and histopathologic evaluation, HE- and virtually stained images were transformed to jp2 format and viewed with JVS view 1.2 freeware[32] or viewed as tiff images in OlyVIA 3.2.1. (Olympus Corporation). For figure representations, snapshots from JVS view, OlyVIA, and LAS X 3.7.4. (Leica Microsystems) were edited with ImageJ Fiji 1.53f51 freeware,[33] and lighting and contrast were adjusted with a linear mode.

Results

Effects of Histologic Processing on Unstained Imaging of Whole Slide Images

To understand how tissue preparation affects the virtual HE staining of WSI tissues, we tested the conditions of tissue section preparation for imaging with visible light (Fig. 1). First, we applied the standard method of imaging tissue sections by just omitting the chemical staining, which entailed removing paraffin,
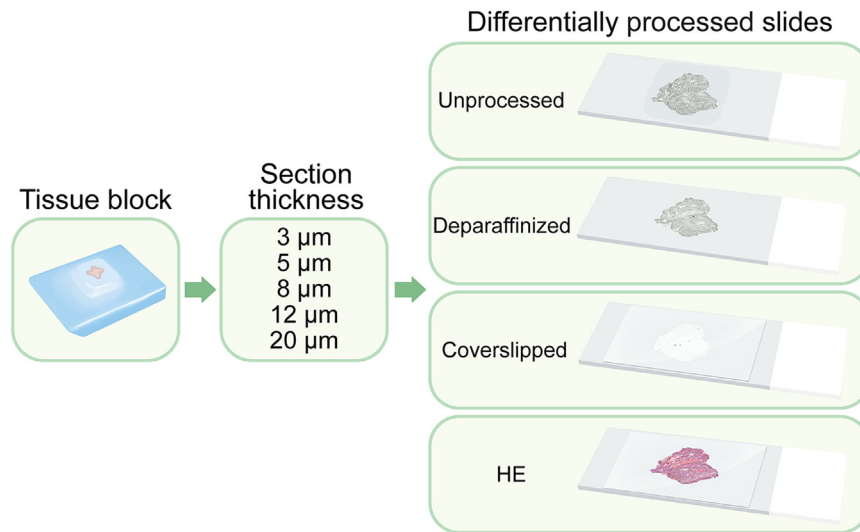
Figure 1.
Conditions of tissue section preparation for WSI with visible light. A paraffin-embedded tissue block was sectioned with 5 different thicknesses for 4 sections each. The sections were then either left unprocessed in paraffin (unprocessed), deparaffinized, coverslipped (including deparaffinization, mounting, and coverslipping), or standardly stained with HE and mounted with a coverslip (HE), 1 for each thickness. The sections were then imaged with visible light as WSIs to be tested for virtual staining. HE, hematoxylin and eosin; WSI, whole slide imaging.

mounting the section with a mounting medium, and covering it with a coverslip (samples referred to as coverslipped). Although this approach was estimated to produce good-quality images as is conventionally the case with any chemically stained tissue sections, the mounting and coverslipping make it challenging to use the same tissue in follow-up approaches owing to potential physical damage during removal of the coverslip and washing away the mounting medium. Hence, we tested whether the mounting and coverslipping could be omitted by using a second approach in which the tissue sections on slides underwent deparaffinization as usual and were imaged directly after that through the air, without a coverslip (samples referred to as deparaffinized). Furthermore, as for certain follow-up methods, such as several spectroscopy techniques, there could be a benefit of tissue sections still residing in the paraffin,[34] we tested a third approach in which the tissue sections attached to glass slides were left untreated and imaged as such, still in paraffin (samples referred to as unprocessed). Then, we compared these 3 unstained imaging approaches with images from chemically HE-stained tissue sections. The 3 unstained sections and the HE reference stainings represented adjacent tissue sections in the following order: HE, coverslipped, deparaffinized, and unprocessed.

In a clinical setting, 4 to 5 μm is the standard thickness for paraffin-embedded tissue sections[35] and is most commonly used with visual interpretation of HE staining. Section thickness affects the information content in the images, and the optimal thickness for the human eye may differ from that of virtual staining development with deep learning. Hence, to test whether thinner or thicker sections provide advantages in virtual staining, we tested 5 different thicknesses of the tissue, 3, 5, 8, 12, and 20 μm, all of which were prepared and imaged with the 3 unstained and 1 HE-stained approach (Fig. 1). After preparing the differentially processed sections, the slides were imaged with standard visible light microscopy. Figure 2 shows the tissue content for each WSI for each condition. It is evident that although the unprocessed and deparaffinized sections provided a well-contrasted signal, the tissue imaged through mounting medium and coverslip exhibited a practically transparent overall appearance to the human eye.

Furthermore, the latter was followed by the appearance of a grid-like pattern in the WSI from the slide scanner fields of imaging. This created a visual pattern based on the field tiling, which was unnoticeable with the other ways of imaging with apparent, higher contrast image content (Fig. 2).

Unsupervised Virtual Staining and Computational Evaluation

Images of all section thickness and preparation condition combinations for unstained imaging were individually used in training and testing the CycleGAN deep learning model (Fig. 3A) with their corresponding chemically stained HE images to produce a virtual HE staining. The images were split to use one half of the WSI for training and the other for testing. To ensure similar content between training and testing data, splitting was performed in a direction that ensured each half of the tissue contained roughly an equal area of all tissue types found in the section. For prostate tissue, this includes glandular structures surrounded by stromal connective tissue, smooth muscle, blood and capillary vessels, and nervous and adipose tissue in the stroma.[36] We evaluated the WSI-level performance of the algorithm by calculating FID scores (Fig. 3B) for each virtual staining. Overall, the FID scores increased with thicker tissues, peaking at 12-μm samples. Comparing the FID scores between different tissue section–processing techniques, deparaffinized samples had the lowest FID scores, and the highest variation was seen with the coverslipped samples. This suggests that the deparaffinized samples may perform slightly better than the unprocessed sections, whereas coverslipped tissue may perform the poorest.

Histologic Evaluation of Unsupervised Virtual Staining

Next, we performed histologic evaluation of the computationally stained sections compared with the reference HE sections. A low magnification view of the overall performance of the virtual staining algorithm with different section preparation techniques
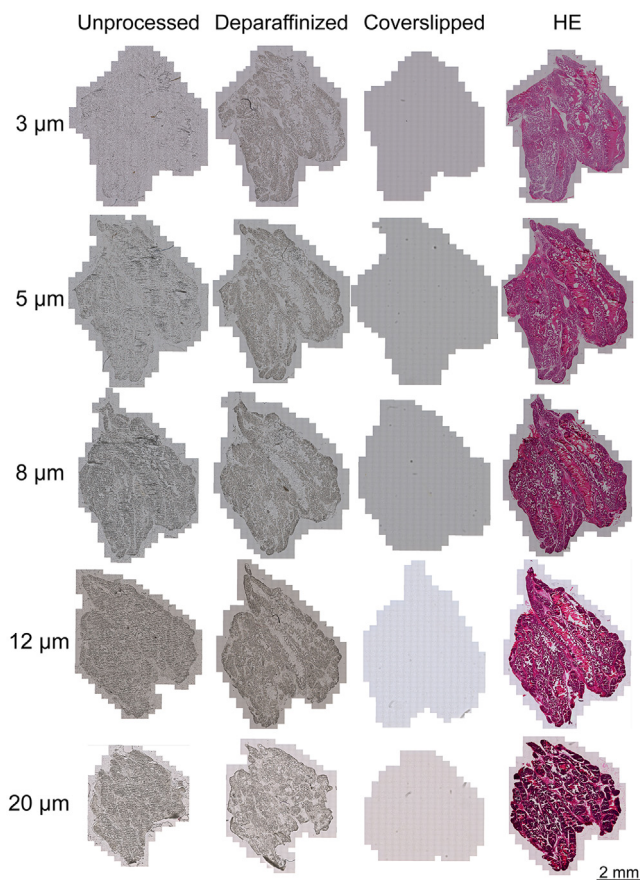
Figure 2.
Tissue content of WSIs imaged for each section-processing condition. WSIs obtained using brightfield microscopy for traditionally, chemically stained HE sections and unstained tissue sections processed differently. The unprocessed and deparaffinized sections provide a well-contrasted signal. The tissue imaged through mounting medium and coverslip (coverslipped) exhibits a practically transparent overall appearance to the human eye, accompanied by the appearance of a grid pattern according to the slide scanner fields of imaging. HE-stained images are for reference. HE, hematoxylin and eosin; WSI, whole slide imaging.
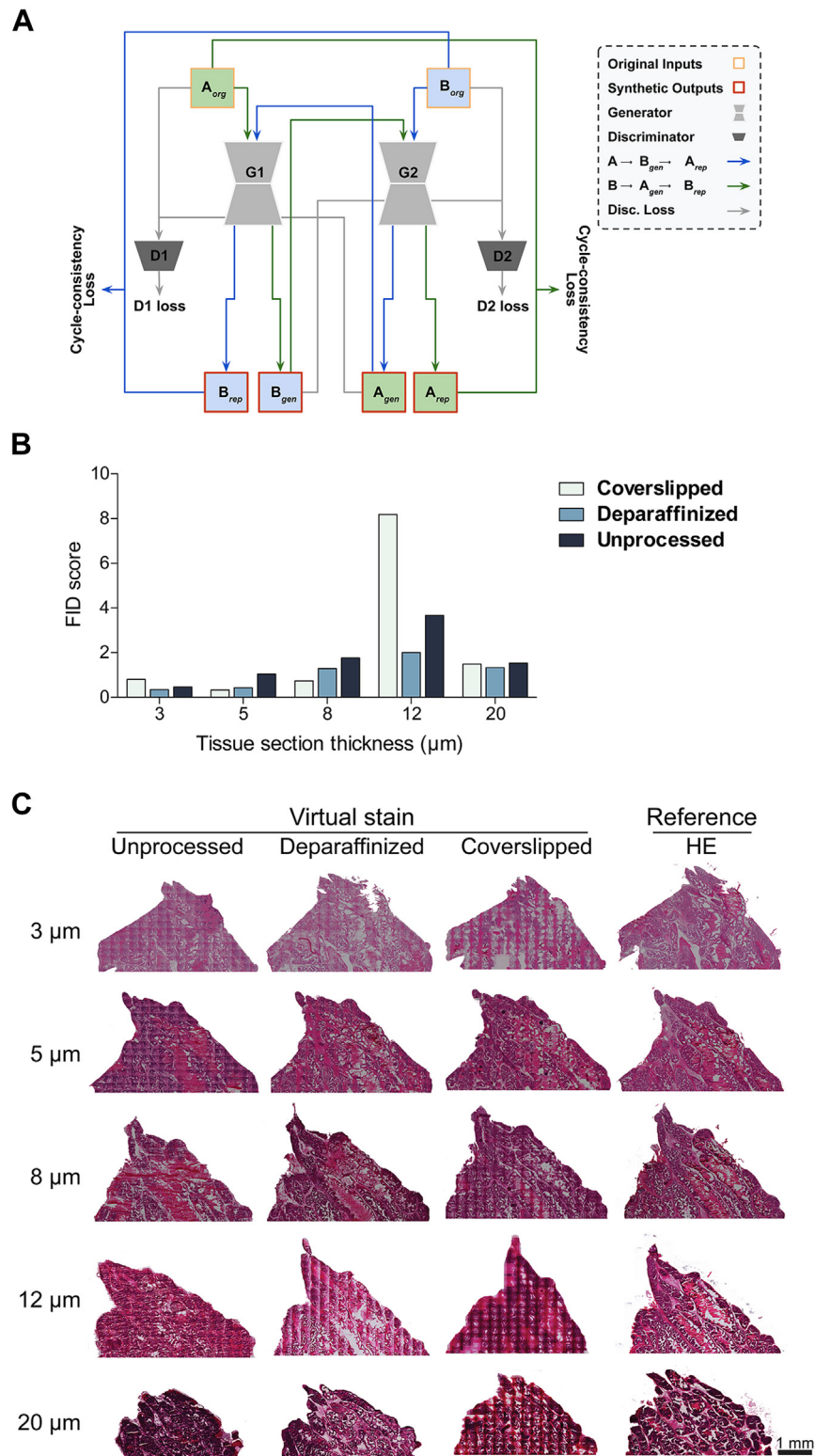
there appeared to be areas that mimicked the images of the reference HE sections almost perfectly in each thickness and processing type; however, the size and proportion of the successful areas varied. In the unprocessed tissues, the nuclei count seemed to either be underrepresented or be exaggerated, and the same effect could be seen in the coverslipped tissues as well. The deparaffinized tissues were the ones performing the best based on the morphology of the epithelium and the nuclei count, which was consistent with the WSI-level results and FID scores (Fig. 4).

The epithelial tissue of the prostate gland is cuboidal to columnar, with abundant, round, and central nuclei. Higher magnifications of the epithelial tissue (Supplementary Fig. S1A) showed that although the epithelial cells themselves were interpreted well by the algorithm, the virtual staining had difficulty with the general morphology of the epithelium with the unprocessed tissues in paraffin as the cells could not be distinguished from each other, especially in the 5-μm- and 8-μm-thick tissues. On the other hand, in the coverslipped and deparaffinized tissues, a rough distinction between cells could be made, although the shape of the cells did not always appear accurate. A common feature that all the 3 virtual stainings shared, when compared with the reference HE, was the absence of inflammatory and basal cells in the lining and periphery of the epithelium, likely resulting from the scarcity of these cells in number compared with the epithelial cells. The same scarcity and the subsequent challenge to be recreated by the virtual staining algorithm also applied to blood vessels, which, in the prostate gland, are mainly small veins or capillaries surrounded by endothelial cells and occasionally containing red blood cells depending on the tissue preparation method. The general structure and shape of the blood vessels were often interpreted well; however, the very thin and elongated endothelial cell nuclei were mostly missing (Supplementary Fig. S1B). Surprisingly, the thinnest tissues performed the best in this respect, and the red blood cells inside the vessels were distinguishable in the coverslipped 3-μm— and 5-μm—thick tissues as well as in the unprocessed 3-μm—thick tissue.

Stroma is the second most abundant tissue found in prostates. It consists of connective tissue and smooth muscle with an eosinophilic cytoplasm and round to thin and elongated nuclei, depending on the orientation of the fibers in the tissue. Similarly to previous findings, 3-μm— and 5-μm—thick tissues performed the best as the organization and color of the fibers were depicted accurately (Supplementary Fig. S2B). Nuclei appeared often either understated or overstated, except in the 3-μm and 5-μm deparaffinized tissues, which showed the most accurate results when taking both nuclei and cytoplasm into consideration. In the 3 thicker tissues, the stroma was not visualized as eosinophilic, and nuclei count was again under- or overestimated. Adipose tissue is a part of connective tissue, and when HE-stained, it appears mainly as hollow circular adipocytes, with peripheral nuclei surrounded by a thin extracellular matrix. Adipocytes were only present in the 3-μm-thick tissue sections in this sample set. Deparaffinized processing produced the best interpretation of them in virtual staining, showing the extracellular matrix and a few of the nuclei most accurately (Supplementary Fig. S2B). The adipocyte nuclei, being small in size and irregular in shape and location, were challenging to reproduce in virtual staining.

Technical Considerations of Unsupervised Virtual Staining

Based on the visual evaluation of the images, several technical issues were identified that affect the performance of virtual HE staining. These include artifacts resulting from optical vignetting,

was consistent with the FID scores, as the thinner sections appeared to perform better than 12-μm- and 20-μm-thick tissues (Fig. 3C). The deparaffinized samples having the lowest FID scores seemed to produce the best results when considering the general morphology of tissue and how hematoxylin and eosin were localized in the virtually stained images compared with the referenced HE sections. The unprocessed samples performed nearly equally, although the remaining paraffin appeared as small creases or folds in the virtually stained tissues, especially in the thicker sections (see below). The images produced from the coverslipped samples had a very pronounced vignetting effect, which overpowered the virtual staining. This was due to the coverslip mounting, making the tissue appear extremely low in contrast, thus causing even the slightest of changes in lighting to substantially stand out in the original unstained tissue. Some vignetting was also apparent with the other processing methods with certain tissue thicknesses (unprocessed, 3-5 μm and deparaffinized, 12 μm). Overall, among the different tissue section thicknesses, 5-μm thickness appeared to perform the best (Fig. 3C).

Next, we investigated whether the WSI-level results were consistent with higher magnification histology (Fig. 4 and Supplementary Figs. S1 and S2). In the virtually stained images,

Figure 3.
Unsupervised virtual HE staining with a CycleGAN deep learning model at a whole slide level. (A) A schematic representation of the CycleGAN network used. The network has 2 generators, G1 and G2, and 2 discriminators, D1 and D2. A_{org} and B_{org} represent original input images from the 2 domains. A_{gen} and B_{gen} represent synthetically generated output images from the original counterparts. A_{rep} and B_{rep} represent repeat synthetically generated images using previously generated B_{gen} and A_{gen}, respectively. Discriminator losses, D1 loss and D2 loss, were computed using original input and generated output. Cycle consistency loss was computed using original input and repeat generated output. (B) Computational evaluation of CycleGAN deep learning model performance with FID scores for each tissue section thickness and processing method. (C) A low magnification view of the overall performance of virtual staining with different tissue section−processing techniques. FID, Frachet inception distance; HE, hematoxylin and eosin.
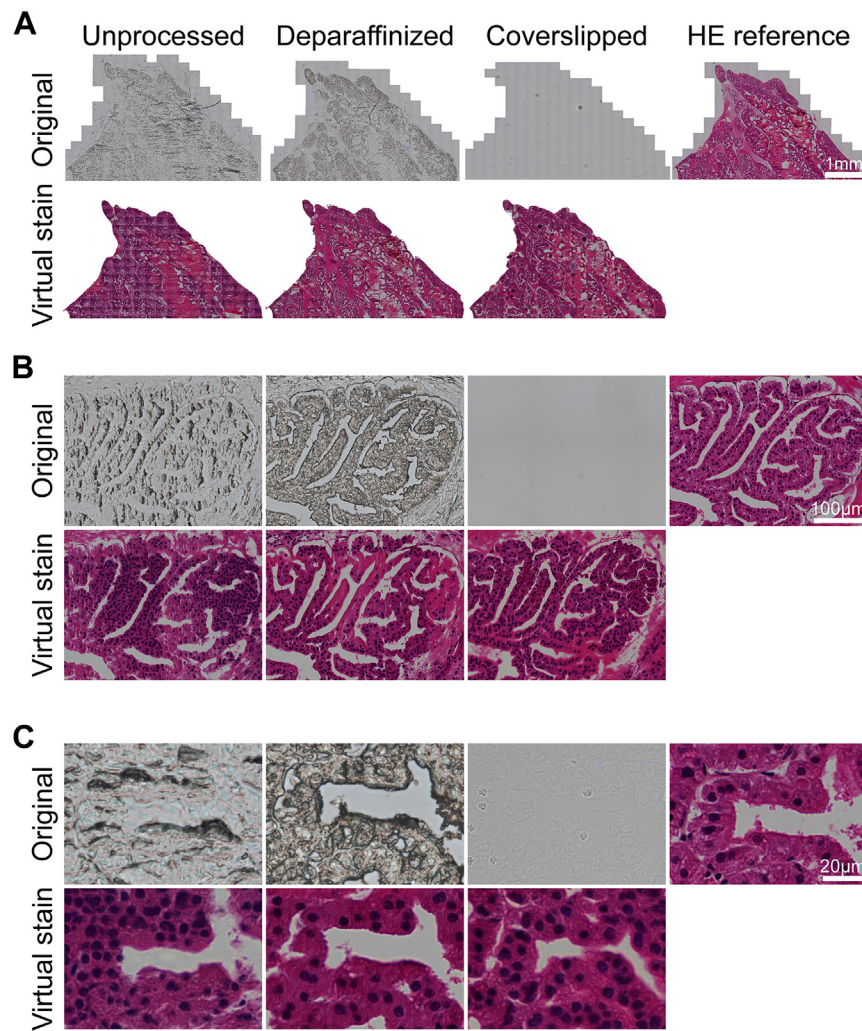
Figure 4.
Histologic performance of unsupervised virtual HE staining with images of differentially processed tissue sections. Comparative views of the original unstained images and virtual staining and HE reference images. An example of section thickness 5 μm is shown. (A) A WSI-level view at low magnification. (B) A view of a prostate gland structure. (C) A high-magnification view of prostate epithelial cells. HE, hematoxylin and eosin; WSI, whole slide imaging.

impurities from the microscope lens, and tiling artifacts from image processing (Supplementary Fig. S3). Optical vignetting is the radial attenuation of light from the center of the image toward the edges, and it is an intrinsic problem of optical systems and digital imaging.[37] This effect, which is distinguishable by the eye from the unstained images only with the coverslipped sections, appeared to be a factor in virtual staining with the other sample processing methods, too. As vignetting is inherent in each microscope and thus embedded in the tiles imaged by the microscope, a pattern of rectangles is easily created by virtual staining. In this study, the virtual staining algorithm interprets vignetting as secretion of the glands (Supplementary Fig. S3A) or denser or darker areas of tissue depending on tissue area.

Depending on their size and the contrast they created, dust particles on the coverslip were also interpreted by the algorithm used in this study (Supplementary Fig. S3B). The more prominent, darker particles created an entirely new tissue structure, whereas the lighter particles seemed to only be interpreted similarly to the vignetting effect, creating an even-colored area similar to the secretion of the glands. In the unprocessed samples, there were creases of paraffin appearing, which became more common with thicker sections. This is most likely a consequence of excess paraffin. These creases were interpreted as nuclei-dense areas and, whereas the glands could be somewhat discerned, the epithelial structure was not represented in virtual staining (Supplementary Fig. S3C). The tile effect (Supplementary Fig. S3D) from splitting the WSIs into 2048 x 2048 pixel tiles for training appeared mostly either on the edges of the tissue or in the secretion of the glands based on visual inspection. This could be related to the high contrast between the sample and the background and, curiously, was more prominent in the coverslipped and unprocessed section images.

Increased Performance of Virtual Staining With an Optimized Imaging Protocol and Supervised Deep Learning

After determining the optimal section thickness and imaging protocol for virtual staining of unstained tissue using the unsupervised deep learning model, we tested whether supervised deep learning could improve the histologic accuracy of virtual staining. We used histologic sections imaged first as
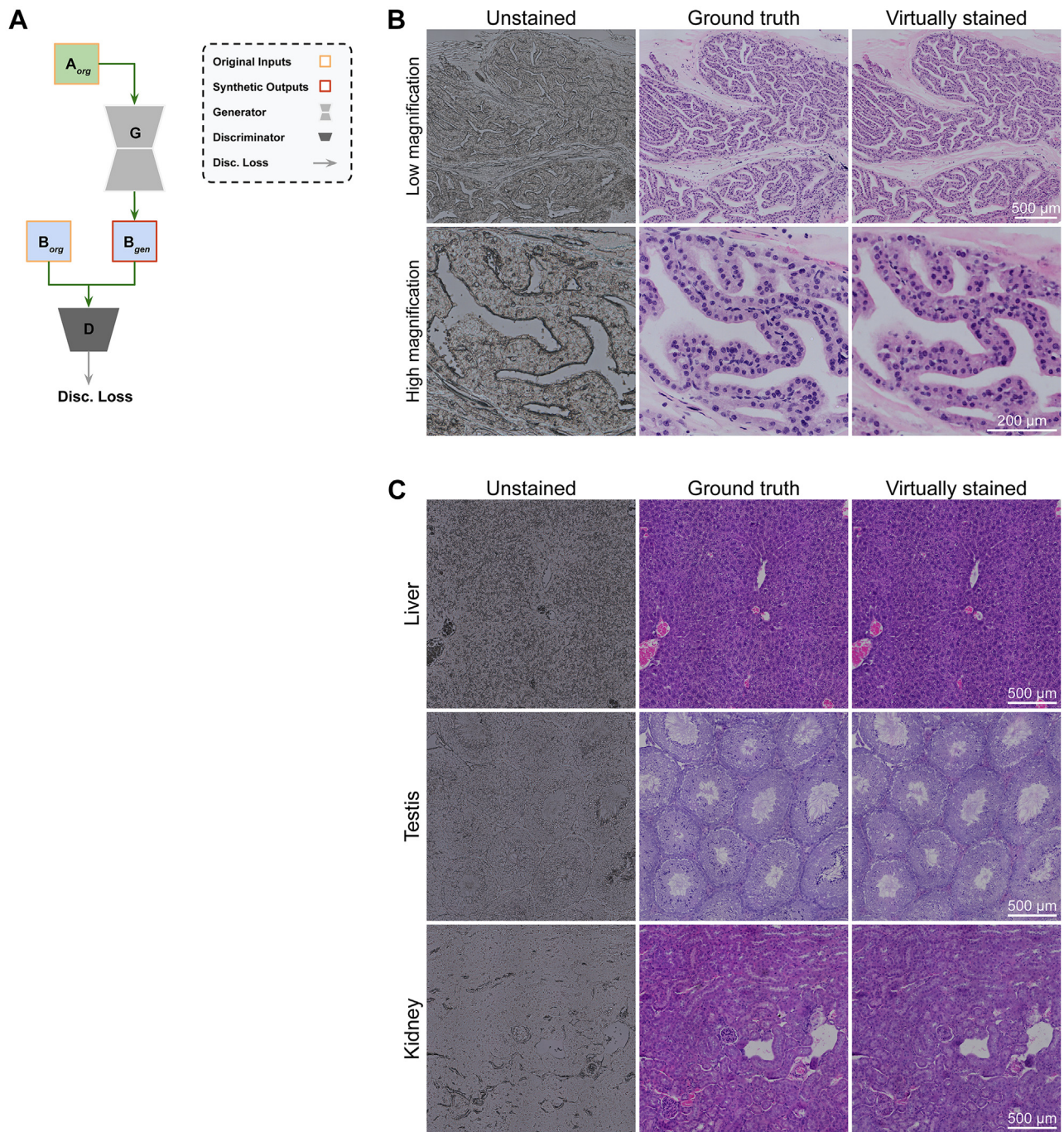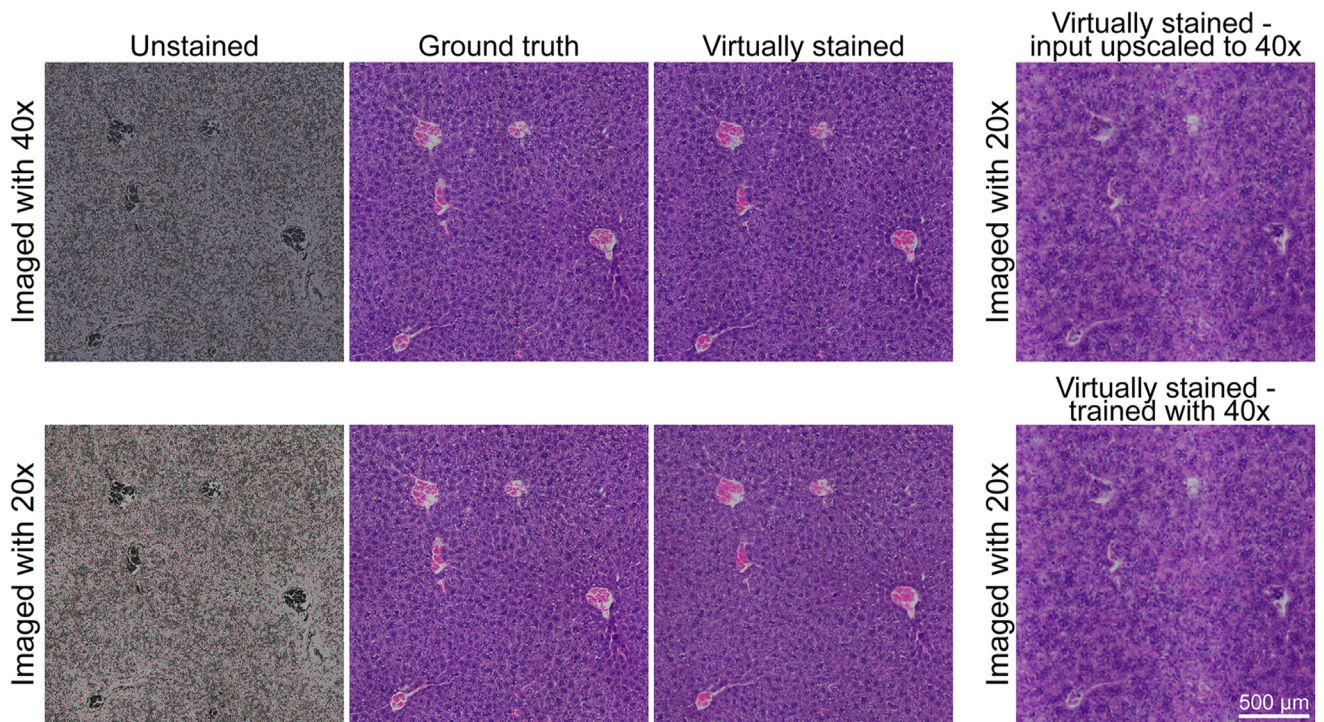
Figure 5.
Supervised virtual HE staining with a pix2pix deep learning model for unstained tissue WSIs. (A) A schematic representation of the pix2pix network. The network has a generator G and a discriminator D. A_{org}, B_{org}, and B_{gen} represent the original input image, the registered ground truth image, and the synthetically generated output, respectively. The network uses a combination of GAN loss and L1 loss for the generator output. (B) Histologic performance of supervised virtual HE staining of prostate gland structures. Comparative views of the original unstained images and virtual staining and HE reference images of prostate gland structure. An overview (top row) and a close-up (bottom row). Basal cell nuclei are indicated using arrowheads. (C) Histologic performance of supervised virtual HE staining of different organ tissues. Comparative views of original unstained images and virtual staining and HE reference images of histology of liver (top row), testis (middle row), and kidney (bottom row). GAN, generative adversial network; HE, hematoxylin and eosin; WSI, whole slide imaging.

deparaffinized without a coverslip to obtain images of the unstained tissue, and then imaged the same section after HE staining to obtain the ground truth image. First, we used mouse prostate tissue and the pix2pix network (Fig. 5A) to evaluate the performance of supervised learning in comparison with the previous results with the unsupervised CycleGAN model. At a low magnification, we found that the general tissue morphology, including that of the stroma and the epithelium-lined glandular structures of the prostate, was interpreted with high accuracy (Fig. 5B). A detailed analysis demonstrated that even basal cells in the

Figure 6.

Histologic performance of supervised virtual HE staining imaged with different magnifications. Comparative views of the original unstained images and virtual staining images with the pix2pix method and the HE reference images. A virtually stained liver was imaged and virtually stained at 40× (top row, 3 images from the left) and 20× (bottom row, 3 images from the left) magnifications. Virtually stained livers were imaged at 20× and virtually stained with a network trained with 40× images (rightmost images) in which the input was upscaled to 40× (top image) and the input remained at 20× (bottom image). HE, hematoxylin and eosin.

epithelium, which were not accurately represented with the unsupervised model, were relatively well reproduced with the supervised model (Fig. 5B).

Next, we tested whether virtual staining could similarly reproduce other tissues with different types of histology. We used samples of the liver, testis, and kidney, and performed virtual staining with the pix2pix model. We found that the general morphology of these tissues was represented well (Fig. 5C). This includes all major structural components, such as the portal regions and hepatic lobules of the liver, seminiferous tubules of the testis, and glomeruli and the cortical tubular epithelium of the kidney, which could be clearly distinguished. Although in the testis, the very basophilic mature spermatozoa appeared more challenging for the algorithm, and the scarce immature spermatogonia and spermatocytes were not shown in virtually stained images, the cellular composition of the liver and the cortical tubular epithelial structures in the kidney appeared highly accurate.

The results thus far have been obtained using a 40× objective in imaging. We wanted to test how the magnification during imaging and training of unstained tissue images affects virtual staining. To this end, we virtually stained images of unstained liver sections that were imaged both with 40× and 20× magnifications using the model trained with 40× and 20× image data, respectively. The performance of virtual staining with the supervised model appeared to be almost equal between the 2 magnifications (Fig. 6). The portal regions and hepatic lobules were both easily distinguishable with both magnifications, although the density of nuclei and overall basophilia of the tissue seemed slightly decreased in the 20× compared with 40× virtually stained images. We further tested how upscaling the input 20× image to 40×

prior to virtual staining affected the results of virtual staining. The accuracy of tissue representation dropped significantly, with the portal regions no longer readily detectable and the hepatocytes appearing considerably larger than accurate (Fig. 6). A similar decrease in representation accuracy was detected when images obtained with 20× magnification were virtually stained with a network trained with images obtained with 40× magnification (Fig. 6).

Discussion

We experimentally optimized and streamlined sample processing and imaging to enable efficient virtual HE staining with CycleGAN, an unsupervised deep learning approach. We compared the effect of tissue section−processing and thickness on the performance of virtual HE staining using images of unstained histologic tissue sections. We showed the feasibility of using unstained tissue sections as deparaffinized or even in paraffin for virtual staining. The benefits of the identified approaches for virtual HE staining include avoiding chemical staining, enabling utilization of the exact same tissue section for other purposes such as macromolecule extractions or various spatial measurements, and providing a fast, cheap, and accessible way to perform future spatial measurements at a single-cell level in concordance with traditional histology.

We explored the different conditions that can be used for unstained tissues, assessing the quality and information content they provide for a virtual staining algorithm. Surprisingly, we found that higher section thicknesses with increased tissue information content in the images do not improve virtual staining results

compared with standard tissue section thicknesses. Clinical histology laboratories often have standardized tissue thicknesses of 4 to 5 μm for an optimized workflow.[35] In this study, the 3 thinner sections that were tested (3-8 μm) performed distinctively better than the 2 thicker sections (12 and 20 μm). Our results showed that the tissue thicknesses used currently for routine chemical HE staining can also be used for virtual staining.

In this study, deparaffinization as the preprocessing technique generated the best virtual staining results both at the WSI level and at the tissue microstructure level. Nuclei count was comparable with the ground truth not only in the abundant epithelial tissues but also in the stromal connective tissue and smooth muscle. Deparaffinized tissues have been reported to be used as unstained tissues in virtual staining.[24,25] Although removing the paraffin and allowing the tissue to dry for microscopy somewhat limit what the tissue can be used for, for most immunohistochemical and histologic staining procedures, the same deparaffinization can be used.

Although not as well performing as the deparaffinized samples, the unprocessed samples showed promise for virtual staining. The strongest benefit of this approach would be that the tissues still embedded in paraffin can be used in practically any follow-up measurement. With certain methods, such as Fourier transform infrared (FTIR) and Raman spectroscopy, the measured signal can even be improved by using unprocessed tissues. In the case of FTIR, resonant Mie scattering distorts the pure spectrum of cells and tissues, especially at the cellular level,[38] and as the refractive indexes of tissue sections and paraffin are similar to each other,[39] the scattering is exacerbated by deparaffinization.[34] A study by Faoláin et al[40] used Raman spectroscopy to examine the effectiveness of the most common deparaffinization agents and found that all of them leave traces of paraffin in tissues. This adds considerable variation to the spectra and prevents automated analysis.[40] Therefore, more precise results at the cellular level can be acquired when tissues are imaged unprocessed, and the paraffin spectra can be computationally subtracted after imaging in both FTIR and Raman spectroscopy.[39,41-43] In addition, a recent study by Sabo et al[44] investigated the use of nondeparaffinized tissue in fluorescence imaging. They highlighted how unprocessed tissue could be used for screening and quality control of tissue sections, thus improving downstream processing and selection of optimal samples.[44] Although the unprocessed sections had drawbacks in virtual staining in this study, namely with under- or overestimating nuclei counts, inability to distinguish cells at the epithelial level, as well as creasing of paraffin at the WSI level, the technical benefits of this approach support the further development of virtual staining algorithms suited for paraffin-embedded sections.

Coverslipped tissues are processed furthest during the histologic workflow, and although the slides are generally not stained after coverslipping owing to the fact that removing the coverslip and further processing can damage the tissue, tissues in fluorescent protocols such as fluorescent immunohistochemistry and in situ hybridization are mounted with coverslips as in HE staining. Still, the staining itself does not appear in visible light. This enables the use of coverslipped slides for virtual staining in combination with fluorescent stainings. The main limitation of using coverslipped slides, however, is the pronounced vignetting effect, which stands out in the virtually stained tissues as darker or incorrectly interpreted tissue. This could be overcome by future development of computationally normalizing the vignetting effect.

Light microscopy is readily available in laboratories using HE staining and is simple to use, making the transition from HE staining to virtual staining of unstained tissue very simple. Nowadays, the workflow in many histopathologic laboratories is automated, and the acquisition of WSIs for pathologic evaluation is often performed with a slide scanner. This requires automatic sample detection and focusing, which may be a challenge for certain types of unstained tissue. The mounting medium in coverslipped tissues has properties that make the tissue almost invisible when using a low magnification. This makes tissue detection extremely difficult. In addition, the remaining paraffin surrounding the tissue in unprocessed, paraffin-embedded tissues could be classified as tissue by the scanner, which would increase the scan time and size of the files significantly, which, in turn, could generate problems for the algorithm. The automatic focus has also been optimized for stained tissues and may need to be readjusted for unstained tissues.

Although the FID score gives an indication of how close an algorithm-generated set of synthetic images is to its corresponding set of real images, whenever paired images are not available, it is still a metric that depends on high level features and does not necessarily gauge low-level visual differences. Hence, the visual assessment of the appearance and performance of virtual staining is crucial. Overall, epithelial tissue does give out the best results, most likely owing to the high abundance and, thus, more prevalence in the training of the algorithm. Eosinophilic areas and structures were more difficult to recreate using the algorithm. This could be caused by the lack of connective tissue and smooth muscle when compared with epithelial tissue. This study also identified technical issues that affect the performance of virtual HE staining, including effects resulting from optical vignetting and impurities from the microscope lens, as well as tiling artifacts from image processing. All these challenges deserve attention in future approaches and are likely to be improved with increased amounts and variations in training data.

Currently, virtual staining of tissues is being applied in several different ways, such as in tissue autofluorescence,[45-47] transforming one stain into another,[14-16,48] normalizing HE staining,[17,18,49] or using a different form of imaging, such as optical imaging.[41-43] Before this study, only a few studies explored traditional light microscopy on unstained tissue for virtual HE staining.[24,25]

In the first part of this study, to avoid tissue damage with the removal of coverslips in the coverslipped samples, the reference HE sections used were obtained from different tissue sections than each of the unstained sections. Hence, an unsupervised approach was used here to compare the feasibility of unstained tissue for virtual HE staining. Unsupervised image-to-image translation methods[5-8] use techniques such as cycle consistency loss[5] for learning image mapping, thus eliminating the need for paired data. However, as the unsupervised methods do not rely on paired data, the ramp-up time is relatively short. Unsupervised networks are often challenging to train because of the typically bulky architecture. Despite being able to generate quality synthetic images for natural domains, the precision may not be as high as with supervised methods.

As supervised learning methods tend to produce more accurate and realistic synthetic images, virtual HE staining can be improved using such approaches. This requires preparing a data set with a high level of pixel-to-pixel correspondence, which, in practice with histologic sections, means imaging the same sections first without and then with chemical staining. Once we had shown that unstained imaging with coverslipping with a mounting medium is not required for efficient information gain from unstained histologic sections, we applied a supervised approach. We showed that increased histologic accuracy can be obtained using supervised

deep learning with an optimized tissue section thickness and imaging protocol. The reproduction of overall tissue histology was clearly improved with supervised learning and pixel-wise ground truth, and we showed that the method works with several tissues with various histology.

We demonstrated that as the resolution was changed prior to virtual staining either by upscaling from 20× to 40× or by using a different magnification in training than as the input, the performance of virtual staining dropped significantly. Surprisingly, however, we found that using images obtained with 20× magnification produces histologic accuracy near to that of images obtained with 40× magnification. In this study, we tested the effect of image resolution with only one tissue. Although the overall morphology of liver and the cellular composition of the tissue-specific structures were well produced, the limitations of each magnification to histologic performance of virtual staining of other tissues and, especially, pathology need to be separately tested.

With these approaches focusing on the usage of deparaffinized and unprocessed tissue sections, and with future development of the algorithms, virtual staining has significant potential to revolutionize the visualization of tissue used in research for standard histologic assessment as well as in combining multiple and spatial measurements. Great future potential of virtual staining also lies in clinical histopathology, with the promise of faster protocols, increased throughputs, and a decreased need for chemical staining steps, with less consumption of environmentally hazardous chemicals.

Author Contributions

P.R. and L.L. designed the study and supervised the work; S.K. and U.K. developed the methodology and provided acquisition and analysis of the data. S.K. and L.L. interpreted the data and wrote the manuscript. All authors reviewed and revised the manuscript, and read and approved the final paper.

Data Availability

Image data used for unsupervised deep learning in this work are freely accessible from the IDA database (www.fairdata.fi/en/ida/) at https://doi.org/10.23729/992968ef-0202-40e9-9a41-cd2c045157b1.

Declaration of Competing Interest

The authors declare no competing interests.

Ethics Approval and Consent to Participate

The mouse tissue material used in the work was collected from the study approved by the board of laboratory animal work of the State Provincial Offices of South Finland (license number: ESAVI/6271/04.10.03/2011).

Supplementary Material

The online version contains supplementary material available at https://doi.org/10.1016/j.labinv.2023.100070.

References

1. Chan JKC. The wonderful colors of the hematoxylin-eosin stain in diagnostic surgical pathology. *Int J Surg Pathol.* 2014;22(1):12–32. https://doi.org/10.1177/1066896913517939
2. Ståhl PL, Salmén F, Vickovic S, et al. Visualization and analysis of gene expression in tissue sections by spatial transcriptomics. *Science.* 2016;353(6294):78–82. https://doi.org/10.1126/science.aaf2403
3. Berglund E, Maaskola J, Schultz N, et al. Spatial maps of prostate cancer transcriptomes reveal an unexplored landscape of heterogeneity. *Nat Commun.* 2018;9(1):2419. https://doi.org/10.1038/s41467-018-04724-5
4. Pang Y, Lin J, Qin T, Chen Z. Image-to-image translation: methods and applications. *IEEE Trans Multimed.* 2022;24:3859–3881. https://doi.org/10.1109/TMM.2021.3109419
5. Zhu JY, Park T, Isola P, Efros AA. Unpaired image-to-image translation using cycle-consistent adversarial networks. Preprint. Posted online March 30, 2017. *Proceedings of the IEEE Int Conf Comput Vis ICCV.* 2017:2223–2232. https://doi.org/10.1109/ICCV.2017.244
6. Liu MY, Breuel T, Kautz J. Unsupervised image-to-image translation networks. Preprint. Posted online March 2, 2017. *Adv Neural Inf Process Syst.* 701-709. https://doi.org/10.48550/arxiv.1703.00848
7. Kim T, Cha M, Kim H, Lee JK, Kim J. Learning to discover cross-domain relations with generative adversarial networks. Preprint. Posted online March 15, 2017. *34th Int Conf Mach Learn ICML.* 2017;4:2941–2949. https://doi.org/10.48550/arxiv.1703.05192
8. Mo S, Cho M, Shin J. InstaGAN: instance-aware image-to-image translation. Preprint. Posted online December 28, 2018. *7th Int Conf Learn Represent ICLR.* 2019. https://doi.org/10.48550/arxiv.1812.10889
9. Goodfellow IJ, Pouget-Abadie J, Mirza M, et al. Generative adversial nets. Preprint. Posted online June 10, 2014. *Adv Neural Inf Process Syst.* 27. https://doi.org/10.1145/3422622
10. Wolterink JM, Dinkla AM, Savenije MHF, Seevinck PR, van den Berg CAT, Išgum I. Deep MR to CT synthesis using unpaired data. *Lect Notes Comput Sci.* 2017;10557:14–23.
11. Yang H, Sun J, Carass A, et al. Unpaired brain MR-to-CT synthesis using a structure-constrained CycleGAN. In: Stoyanov D, Taylor Z, Carneiro G, et al., eds. *Deep Learning in Medical Image Analysis and Multimodal Learning for Clinical Decision Support.* Cham: Springer; 2018:174–182.
12. Yang H, Sun J, Carass A, et al. Unsupervised MR-to-CT synthesis using structure-constrained CycleGAN. *IEEE Trans Med Imaging.* 2020;39(12):4249–4261. https://doi.org/10.1109/TMI.2020.3015379
13. Liu Y, Chen A, Shi H, et al. CT synthesis from MRI using multi-cycle GAN for head-and-neck radiation therapy. *Comput Med Imaging Graph.* 2021;91, 101953. https://doi.org/10.1016/J.COMPMEDIMAG.2021.101953
14. Xu Z, Huang X, Moro CF, Bozóky B, Zhang Q. GAN-based virtual re-staining: a promising solution for whole slide image analysis. Preprint. Posted online January 13, 2019. https://doi.org/10.48550/arxiv.1901.04059
15. Liu S, Zhang B, Liu Y, et al. Unpaired stain transfer using pathology-consistent constrained generative adversarial networks. *IEEE Trans Med Imaging.* 2021;40(8):1977–1989. https://doi.org/10.1109/TMI.2021.3069874
16. Levy JJ, Azizgolshani N, Andersen MJ, et al. A large-scale internal validation study of unsupervised virtual trichrome staining technologies on

nonalcoholic steatohepatitis liver biopsies. *Mod Pathol.* 2021;34(4):808−822. https://doi.org/10.1038/s41379-020-00718-1

17. de Bel T, Hermsen M, Kers J, van der Laak J, Litjens G. Stain-transforming cycle-consistent generative adversarial networks for improved segmentation of renal histopathology. In: Cardoso MJ, Feragen A, Glocker B, et al., eds. *Proceedings of the 2nd International Conference on Medical Imaging With Deep Learning; vol 102.* Proceedings of Machine Learning Research; 2019:151−163.

18. de Bel T, Bokhorst JM, van der Laak J, Litjens G. Residual cyclegan for robust domain transformation of histopathological tissue slides. *Med Image Anal.* 2021;70, 102004. https://doi.org/10.1016/J.MEDIA.2021.102004

19. Isola P, Zhu JY, Zhou T, Efros AA. Image-to-image translation with conditional adversarial networks. *Proc-30th IEEE Conf Comput Vis Pattern Recognit CVPR 2017.* 2017:5967−5976. https://doi.org/10.1109/CVPR.2017.632

20. Park T, Liu MY, Wang TC, Zhu JY. Semantic image synthesis with spatially-adaptive normalization. *Proceedings of the IEEE Comput Soc Conf Comput Vis Pattern Recognit.* 2019:2332−2341. https://doi.org/10.48550/arxiv.1903.07291

21. Wang TC, Liu MY, Zhu JY, Tao A, Kautz J, Catanzaro B. High-resolution image synthesis and semantic manipulation with conditional GANs. *Proc IEEE Comput Soc Conf Comput Vis Pattern Recognit.* 2017:8798−8807. https://doi.org/10.48550/arxiv.1711.11585

22. Zhu P, Abdal R, Qin Y, Wonka P. SEAN: image synthesis with semantic region-adaptive normalization. *Proc IEEE Comput Soc Conf Comput Vis Pattern Recognit.* 2019:5103−5112. https://doi.org/10.1109/CVPR42600.2020.00515

23. Zitová B, Flusser J. Image registration methods: a survey. *Image Vis Comput.* 2003;21(11):977−1000. https://doi.org/10.1016/S0262-8856(03)00137-9

24. Rana A, Yauney G, Lowe A, Shah P. Computational histological staining and destaining of prostate core biopsy RGB images with generative adversarial neural networks. *2018 17th IEEE Int Conf Mach Learn Appl.* 2018:828−824. https://doi.org/10.1109/ICMLA.2018.00133

25. Rana A, Lowe A, Lithgow M, et al. Use of deep learning to develop and analyze computational hematoxylin and eosin staining of prostate core biopsy images for tumor diagnosis. *JAMA Netw Open.* 2020;3(5):e205111. https://doi.org/10.1001/jamanetworkopen.2020.5111

26. Latonen L, Scaravilli M, Gillen A, et al. In vivo expression of miR-32 induces proliferation in prostate epithelium. *Am J Pathol.* 2017;187(11):2546−2557. https://doi.org/10.1016/j.ajpath.2017.07.012

27. Ruusuvuori P, Valkonen M, Nykter M, Visakorpi T, Latonen L. Feature-based analysis of mouse prostatic intraepithelial neoplasia in histological tissue sections. *J Pathol Inform.* 2016;7:5. https://doi.org/10.4103/2153-3539.175378

28. Valkonen M, Ruusuvuori P, Kartasalo K, Nykter M, Visakorpi T, Latonen L. Analysis of spatial heterogeneity in normal epithelium and preneoplastic alterations in mouse prostate tumor models. *Sci Rep.* 2017;7:44831. https://doi.org/10.1038/srep44831

29. Heusel M, Ramsauer H, Unterthiner T, Nessler B, Hochreiter S. GANs trained by a two time-scale update rule converge to a local Nash equilibrium. In: *Proceedings of the 31st International Conference on Neural Information Processing Systems. NIPS'17.* Curran Associates Inc; 2017:6629−6640.

30. Szegedy C, Liu W, Jia Y, et al. Going deeper with convolutions. Preprint. Posted online September 17, 2014. *Proc IEEE Comput Soc Conf Comput Vis Pattern Recognit.* https://doi.org/10.48550/arxiv.1409.4842

31. Ronneberger O, Fischer P, Brox T. U-Net: convolutional networks for biomedical image segmentation. In: Navab N, Hornegger J, Wells WM, Frangi AF, eds. *Medical Image Computing and Computer-Assisted Intervention−MICCAI 2015. Lecture Notes in Computer Science.* Springer International Publishing; 2015:234−241. https://doi.org/10.1007/978-3-319-24574-4_28

32. Tuominen VJ, Isola J. The application of JPEG2000 in virtual microscopy. *J Digit Imaging.* 2009;22(3):250−258. https://doi.org/10.1007/S10278-007-9090-Z

33. Schindelin J, Arganda-Carreras I, Frise E, et al. Fiji: an open-source platform for biological-image analysis. *Nat Methods.* 2012;9(7):676−682. https://doi.org/10.1038/nmeth.2019

34. Pilling M, Gardner P. Fundamental developments in infrared spectroscopic imaging for biomedical applications. *Chem Soc Rev.* 2016;45(7):1935−1957. https://doi.org/10.1039/C5CS00846H

35. Masuda S, Suzuki R, Kitano Y, et al. Tissue thickness interferes with the estimation of the immunohistochemical intensity: introduction of a control system for managing tissue thickness. *Appl Immunohistochem Mol Morphol.* 2021;29(2):118−126. https://doi.org/10.1097/PAI.0000000000000859

36. Knoblaugh S, True L. Male reproductive system. In: Treuting P, Dintzis S, Liggitt D, eds. *Comparative Anatomy and Histology: A Mouse and Human Atlas.* Elsevier/Academic Press; 2011:285−308.

37. Piccinini F, Lucarelli E, Gherardi A, Bevilacqua A. Multi-image based method to correct vignetting effect in light microscopy images. *J Microsc.* 2012;248(1):6−22. https://doi.org/10.1111/j.1365-2818.2012.03645.x

38. Bassan P, Kohler A, Martens H, et al. RMieS-EMSC correction for infrared spectra of biological cells: extension using full Mie theory and GPU computing. *J Biophotonics.* 2010;3(8-9):609−620. https://doi.org/10.1002/JBIO.201000036

39. De Lima FA, Gobinet C, Sockalingum G, et al. Digital de-waxing on FTIR images. *Analyst.* 2017;142(8):1358−1370. https://doi.org/10.1039/C6AN01975G

40. Faoláin EO, Hunter MB, Byrne JM, et al. Raman spectroscopic evaluation of efficacy of current paraffin wax section dewaxing agents. *J Histochem Cytochem.* 2005;53(1):121−129. https://doi.org/10.1177/002215540505300114

41. Ibrahim O, Toner M, Flint S, Byrne HJ, Lyng FM. The potential of Raman spectroscopy in the diagnosis of dysplastic and malignant oral lesions. *Cancers.* 2021;13(4):1−14. https://doi.org/10.3390/CANCERS13040619

42. Nallala J, Diebold MD, Gobinet C, et al. Infrared spectral histopathology for cancer diagnosis: a novel approach for automated pattern recognition of colon adenocarcinoma. *Analyst.* 2014;139(16):4005−4015. https://doi.org/10.1039/C3AN01022H

43. Nguyen TNQ, Jeannesson P, Groh A, Piot O, Guenot D, Gobinet C. Fully unsupervised inter-individual IR spectral histology of paraffinized tissue sections of normal colon. *J Biophotonics.* 2016;9(5):521−532. https://doi.org/10.1002/JBIO.201500285

44. Sabo AR, Winfree S, Bledsoe SB, et al. Label-free imaging of non-deparaffinized sections of the human kidney to determine tissue quality and signatures of disease. *Physiol Rep.* 2022;10(3):e15167. https://doi.org/10.14814/PHY2.15167

45. Meng X, Li X, Wang X. A computationally virtual histological staining method to ovarian cancer tissue by deep generative adversarial networks. *Comput Math Methods Med.* 2021;2021:4244157. https://doi.org/10.1155/2021/4244157

46. Picon A, Medela A, Sánchez-Peralta LF, et al. Autofluorescence image reconstruction and virtual staining for in-vivo optical biopsying. *IEEE Access.* 2021;9:32081−32093. https://doi.org/10.1109/ACCESS.2021.3060926

47. Rivenson Y, Wang H, Wei Z, et al. Virtual histological staining of unlabelled tissue-autofluorescence images via deep learning. *Nat Biomed Eng.* 2019;3(6):466−477. https://doi.org/10.1038/s41551-019-0362-y

48. de Haan K, Zhang Y, Zuckerman JE, et al. Deep learning-based transformation of H&E stained tissues into special stains. *Nat Commun.* 2021;12(1):4884. https://doi.org/10.1038/s41467-021-25221-2

49. Tosta TAA, de Faria PR, Servato JPS, et al. Unsupervised method for normalization of hematoxylin-eosin stain in histological images. *Comput Med Imaging Graph.* 2019;77:101646. https://doi.org/10.1016/j.compmedimag.2019.101646